01 Jan 2023

Development and Assessment of Magnetic Fe2O3@MOF-74 Composite Sorbents for Ethylene/ethane Separation

Khaled Baamran

Kyle Newport

Ali A. Rownaghi
Missouri University of Science and Technology, rownaghia@mst.edu

Fateme Rezaei
Missouri University of Science and Technology, rezaeif@mst.edu

Development and assessment of magnetic Fe$_2$O$_3$@MOF-74 composite sorbents for ethylene/ethane separation

Khaled Baamran, Kyle Newport, Ali A. Rownaghi, Fateme Rezaei [*]

Department of Chemical & Biochemical Engineering, Missouri University of Science and Technology, 1101 N State Street, Rolla, MO 65409, United States

A B S T R A C T

Development of smart sorbents that can be regenerated when triggered by external stimuli such as magnetic field can overcome the poor energy utilization of the current sorbents investigated for light olefins/paraffins separation. In this work, we report the development of novel magnetic sorbents comprising of MOF-74 crystals and superparamagnetic Fe$_2$O$_3$ particles in a core–shell structure, and assessment of their C$_2$H$_4$/C$_2$H$_6$ separation performance. The electromagnetic properties of the materials were tuned by varying the Fe$_2$O$_3$ (Fe$_x$) loading (x = 1–20 wt%), and their effects on adsorption capacity, selectivity, and desorption rates were systematically investigated. The surface area, microporosity, and the C$_2$H$_4$/C$_2$H$_6$ selectivity of composites were reduced as the Fe$_x$ content increased, while the specific heat absorption rate (SAR) was increased from 60 to 80 % upon varying the magnetic field intensity from 12.6 to 31.4 mT. On the basis of the SAR enhancement upon increasing the Fe$_x$ loading, the C$_2$H$_4$ desorption rates were gradually increased with Fe$_x$ up to 10 wt%, however beyond this composition a decline in the desorption rates was noted. Moreover, the cooling rate was found to be ~76 % higher in induction heating compared to the conventional thermal heating method, which is expected to significantly shorten the cycle time, thereby reducing the column size and improving the throughput of the system. Our results highlight the importance of assessing the trade-offs between capture capacity and extent of responsiveness to magnetic field (i.e., temperature rise during regeneration) when developing smart sorbents. This work builds on previous studies that demonstrate the suitability of novel stimuli-responsive sorbents for next generation of olefin/paraffin separation systems.

1. Introduction

Ethylene (C$_2$H$_4$), which is typically produced by thermal decomposition or steam reforming of ethane (C$_2$H$_6$), is one of the most important feedstocks in chemical industry with a global annual production of over 170 million tons [1–4]. A downstream cryogenic distillation is usually needed to purify the produced C$_2$H$_4$ by removing small residue of co-existed C$_2$H$_6$ in the product [5–8]. This legacy separation process is extremely energy intensive and therefore, significant efforts have been put forth to replace it with other non-thermal driven separations like membrane or adsorption [9–12]. In particular, adsorptive separation over nanoporous materials has been regarded as a promising technology for C$_2$H$_4$/C$_2$H$_6$ separation [13,14]. Despite significant advances made in sorbents design and discovery over the past few decades, adsorptive separation of light olefins/paraffins has still a long way to go toward commercialization.

Electrification of separation processes requires departure from conventional pressure/temperature swing adsorption (P/TSA) systems that require high energy input to regenerate the sorbent. In this regard, alternative approaches such as electric swing adsorption (ESA), microwave swing adsorption (MSA), and magnetic induction swing adsorption (MISA) that are based on converting electricity into heat using Joule heating, microwave heating, and induction heating, respectively, have been proposed recently [15–18]. In the ESA process, the ohmic resistance of sorbent converts electricity to heat during desorption step. The electric current needs to be evenly distributed over the sorbent bed for efficient heating, which necessitates uniform connectivity along the bed. In case of maldistribution, poor electric conductivity can generate hot spots, which makes ESA unsafe. Thus, scaling up the ESA process becomes extremely challenging [19,20]. Contrary to ESA, the sorbent in MSA or MISA process does not need connectivity or uniform distribution along the bed and can be heated up remotely as long as the sorbent has the capability to be heated under microwave irradiation or magnetic induction. The induction heating technology has recently grabbed
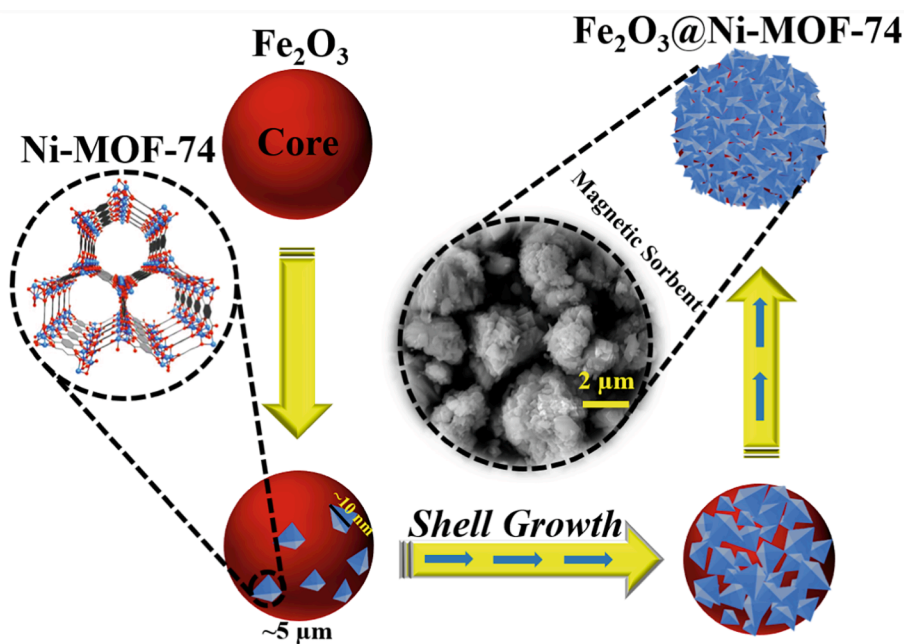
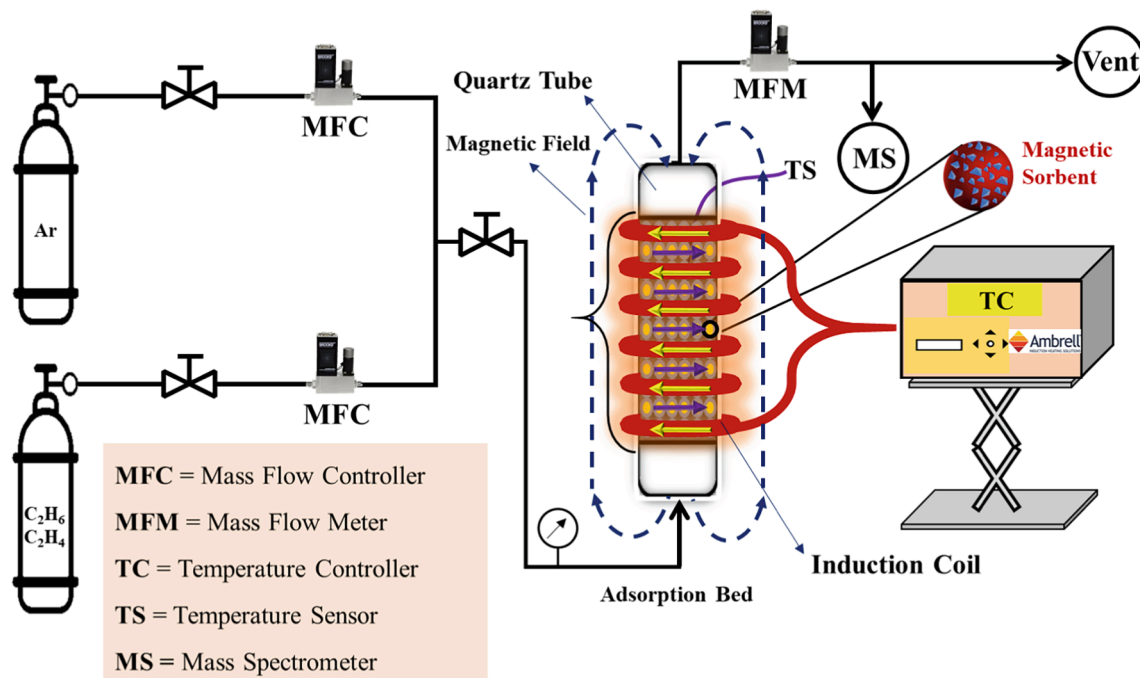**Fig. 1.** Schematic demonstration of Fe$_x$@MOF composites synthesis.

Fig. 2. Schematic of the experimental setup used in magnetic induction experiments.

researchers' interest to find its way toward electrification of separation processes in the chemical industry.

In induction heating, changing the magnetic field via applying high frequency currents induces the eddy currents and alternates the direction of magnetically aligned domains, causing a rise in temperature, and hence gas desorption and sorbent regeneration. This phenomenon typically occurs either by the magnetic dissipation or ohmic resistance [19,21]. In this method, heat is generated by dynamic core losses and static hysteresis of ferrimagnetic particles induced by an external current magnetic field (CMF); this makes the heating zone concentrated within the induction coil length, thereby making the cooling step much shorter compared to the conventional heating in TSA [18,22]. A

daunting challenge in implementing this technology is poor electromagnetic conductivity of the sorbents, which renders the materials unresponsive to the applied magnetic field. To address this issue, hybridization of sorbent crystals and magnetic particles has been attempted, aiming at enhancing the local thermal heating of sorbent particles via exposing them to an alternating CMF. For instance, Hill and co-workers reported the use of induction heating for CO$_2$ desorption over composites of MOF crystals (e.g., UiO-66 and Mg-MOF-74) and ferrimagnetic MgFe$_2$O$_4$ [18,22,23]. The authors reported 100 % CO$_2$ release over UiO-66@MgFe$_2$O$_4$ sorbent with a thermal efficiency of ~60 % during 240 s regeneration time at 42 mT. Using Mg-MOF-74/ MgFe$_2$O$_4$, a CO$_2$ release efficiency of ~67.3 % was observed within 21
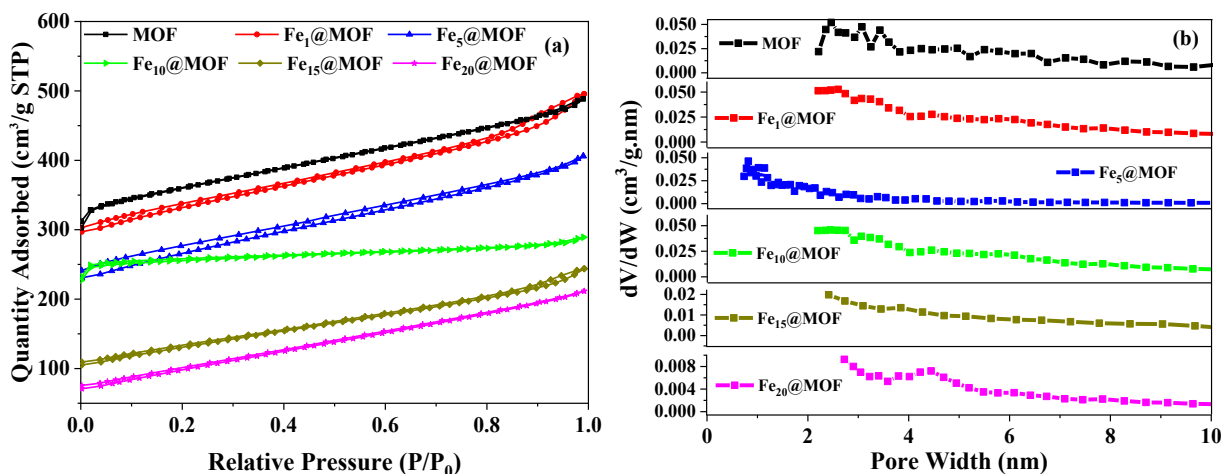
Fig. 3. (a) N_2 physisorption isotherms and (b) PSD profiles of the Fe$_x$@MOF composites.

Table 1
Textural properties of the bare MOF and the corresponding Fe$_x$@MOF composites.

Sorbent	S_{BET} (m^2/g)	V_{micro} (cm^3/g)	V_{meso} (cm^3/g)	d_p (nm)
Fe$_2$O$_3$	11	0.00	0.03	5, 7.5, 11
MOF	1207	0.41	0.15	2.3, 2.5, 2.6
Fe$_1$@MOF	1117	0.39	0.17	2.4, 2.5, 2.7, 3.5
Fe$_5$@MOF	930	0.36	0.14	2.4, 2.5, 2.6, 3.1
Fe$_{10}$@MOF	877	0.23	0.16	2.4, 2.5, 2.6, 3.2
Fe$_{15}$@MOF	453	0.08	0.12	2.5, 2.6, 3.1, 3.4
Fe$_{20}$@MOF	351	0.01	0.13	2.6, 2.8, 3.2, 3.7

min at 55.9 mT. In another investigation, Lin et al. [24] applied the concept of induction heating for release of CO_2 from amine-functionalized mesoporous carbon, incorporated with Fe$_3$O$_4$ as suscep-tors. Their process achieved a desorption rate and an efficiency of 3.27 mg/g.s and 79.2 %, respectively, which outperformed the conventional convective heat transfer-based TSA process. Most recently, Denayer group reported fast thermal regeneration of extrudates of 13X/Fe$_3$O$_4$ composites when exposed to CMF [19]. Their composite with 20 wt% Fe$_3$O$_4$ was shown to absorb almost twice the net energy of its counter-part composite with 10 wt% of Fe$_3$O$_4$, with much higher desorption rate.

As we make transition to a clean energy future, we need to reduce the dependency of adsorptive separation to thermal energy. In that regard, MISA appears to be a promising technology for electrification of light olefins/paraffins separation. The objective of this work was to develop magnetic-responsive sorbents, that can be regenerated upon exposure to an external magnetic field, for separation of ethane and ethylene. Five different composite sorbents comprising of Ni-MOF-74 and Fe$_2$O$_3$ (Fe$_x$@MOF, where x = 1, 5, 10, 15, and 20 wt%) were developed and characterized via various tools. The unary adsorption isotherms of C_2H_4 and C_2H_6 were measured to estimate the adsorption capacity of the synthesized materials and to estimate the ideal adsorbed solution theory (IAST) selectivities. Dynamic adsorption–desorption experiments were then conducted using binary C_2H_4/C_2H_6 feed to systematically assess the effect of magnetic field induction effectiveness on thermal efficiency, desorption rate, and cooling rate enhancement under varied magnetic field strengths (12.6, 21.4, 31.4 mT). The relationships between mate-rials properties and performance were established for Fe$_x$@MOF with core-shell structure and varied composition.

2. Experimental section

2.1. Materials

Chemicals used in the synthesis such as tetrahydrofuran (THF, 99.9 %) and ethanol (EtOH, 99.9 %) were purchased from the commercial vendors and used without further purification. Nickel (II) acetate tet-rahydrate (Ni(AC)$_2$·4H$_2$O, 99 %), 2,5-dihydroxyterephthalic acid (DHTA, 98 %), and iron oxide microparticle (Fe$_2$O$_3$, alpha, 99.5 %, < 5 μm) were obtained from Sigma-Aldrich. All ultrahigh-purity gases used in this study were purchased from Airgas.

2.2. Synthesis of Ni-MOF-74

Ni-MOF-74 was synthesized using a well-established solvothermal procedure described elsewhere [25]. Briefly, the MOF synthesis liquor was prepared by dissolving 0.374 g of Ni(AC)$_2$·4H$_2$O in 35 mL of DI water, and 0.158 g of DHTA in 35 mL of THF. The two solutions were sonicated separately for 30 min, followed by another 10-min sonication when both solutions were combined. Then, the solution was stirred for 30 min using magnetic stirrer before it was transferred to a Teflon-lined autoclave and heated to 110 °C for 3 days. After cooling to room tem-perature, the yellowish fine crystalline powder was filtered and washed by EtOH. To remove unreacted precursors, the powder was immersed in EtOH for 3 days, in which EtOH was replaced daily. The material was then filtered and activated under vacuum at 150 °C for 18 h, followed by 3 h activation at 200 °C.

2.3. Synthesis of Fe$_x$@Ni-MOF-74 composites

The synthesis of magnetic composites with core–shell structure was followed the procedures reported in the literature [25,26]. The Fe$_2$O$_3$ content was varied from 1 to 20 % of the weight of the initial Ni pre-cursor (Fe$_x$, where x = 1, 5, 10, 15, and 20 wt%). The only difference between synthesizing a pristine MOF and a magnetic composite was the step of dissolving Ni(AC)$_2$·4H$_2$O in 35 mL of DI water, in which the required amount of Fe$_2$O$_3$ (Fe$_1$, Fe$_5$, Fe$_{10}$, Fe$_{15}$, or Fe$_{20}$) was dissolved simultaneously with Ni precursor in DI water before it was sealed in a Teflon-lined autoclave and reacted at 110 °C for 3 days to initiate a core–shell growth, as schematically depicted in Fig. 1. After cooling, the dark red crystalline powder was filtered and washed by EtOH. To remove unreacted species, the powder was immersed in EtOH for 3 days while EtOH was replaced daily. The materials were filtered and acti-vated under vacuum at 150 °C for 18 h, followed by 3 h activation at 200 °C, similar to the pristine Ni-MOF-74. Throughout the paper, the pristine Ni-MOF-74 and the magnetic composites are referred to as MOF
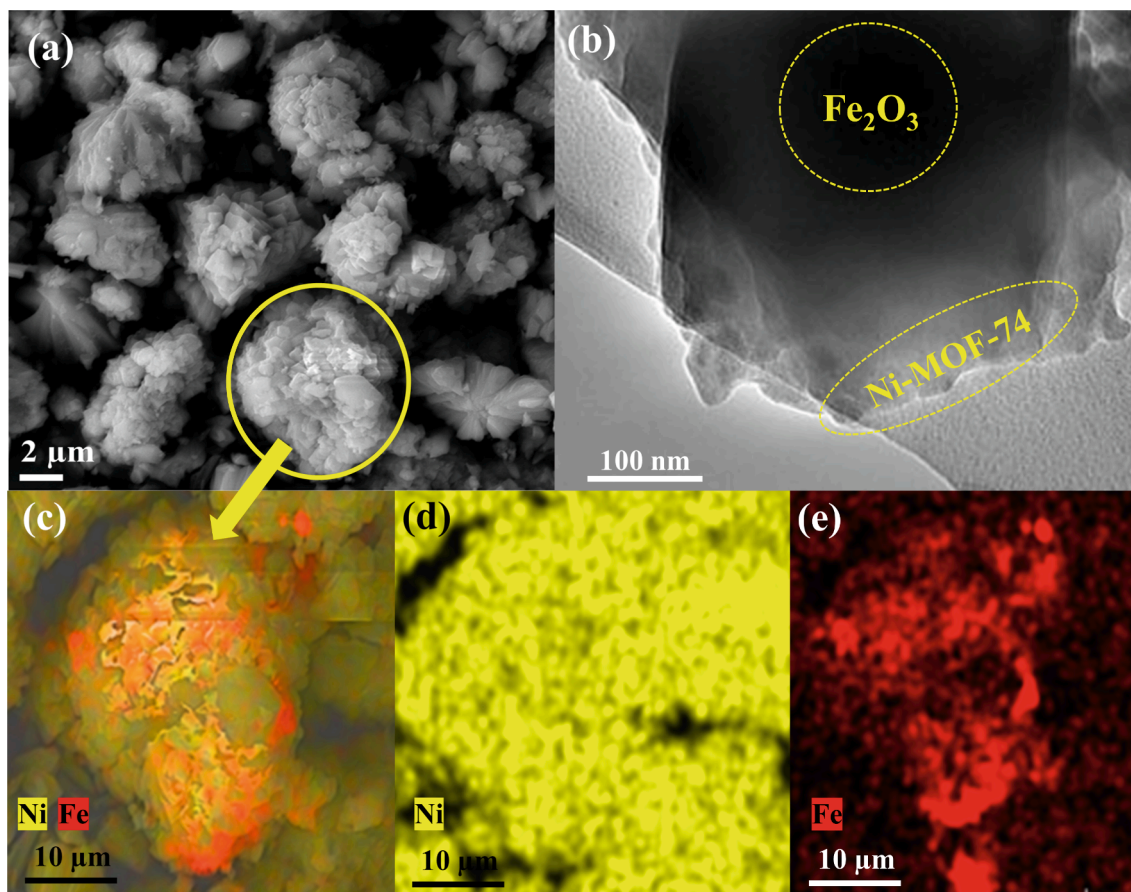
Fig. 4. (a) SEM image, (b) TEM image, and (c-e) EDX mapping of Fe_1@MOF.
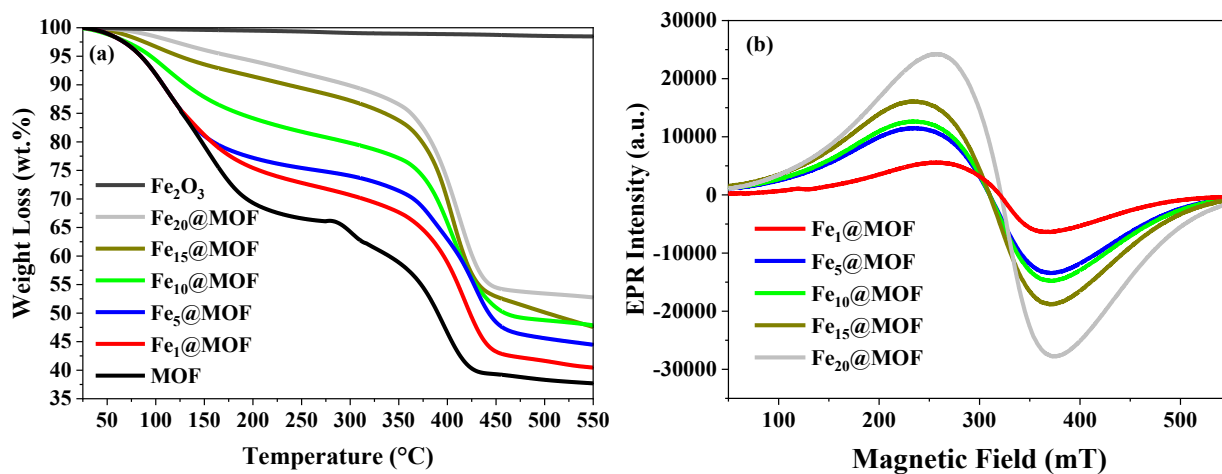
Fig. 5. (a) TGA profiles and (b) EPR spectra of the Fe_x@MOF composites.

Table 2
SAR of magnetic particles with varied composition (wt%) at different magnetic field strengths.

Current (mT)	Frequency (kHz)	SAR (W/g)				
		Fe_1	Fe_5	Fe_{10}	Fe_{15}	Fe_{20}
12.6	190	1.86	3.69	4.21	4.94	9.20
21.4	190	10.86	11.68	12.65	14.83	19.75
31.4	190	24.45	30.02	32.86	37.59	60.27

andFe_1@MOF, Fe_5@MOF, Fe_{10}@MOF, Fe_{15}@MOF, and Fe_{20}@MOF, respectively.

2.4. Characterization of Fe_x@MOF composites

N_2 physisorption tests at 77 K were carried out on a Micromeritics (3Flex) gas analyzer instrument to evaluate the textural properties of the Fe_x@MOF composites. Prior to the measurements, MOF, Fe_1@MOF, Fe_5@MOF, Fe_{10}@MOF, Fe_{15}@MOF, and Fe_{20}@MOF were degassed on a Micromeritics Smart VacPrep instrument at 120 °C under vacuum for 5

Fig. 6. Unary adsorption isotherms of (a) C_2H_6 and (b) C_2H_4 for the bare MOF and the corresponding Fe_x@MOF composites at 25 °C.

h. The nonlocal density functional theory (NLDFT), Horvath and Kawazoe, and Brunauer–Emmett–Teller (BET) methods were utilized to estimate the pore volume, pore size distribution (PSD), and surface area, resp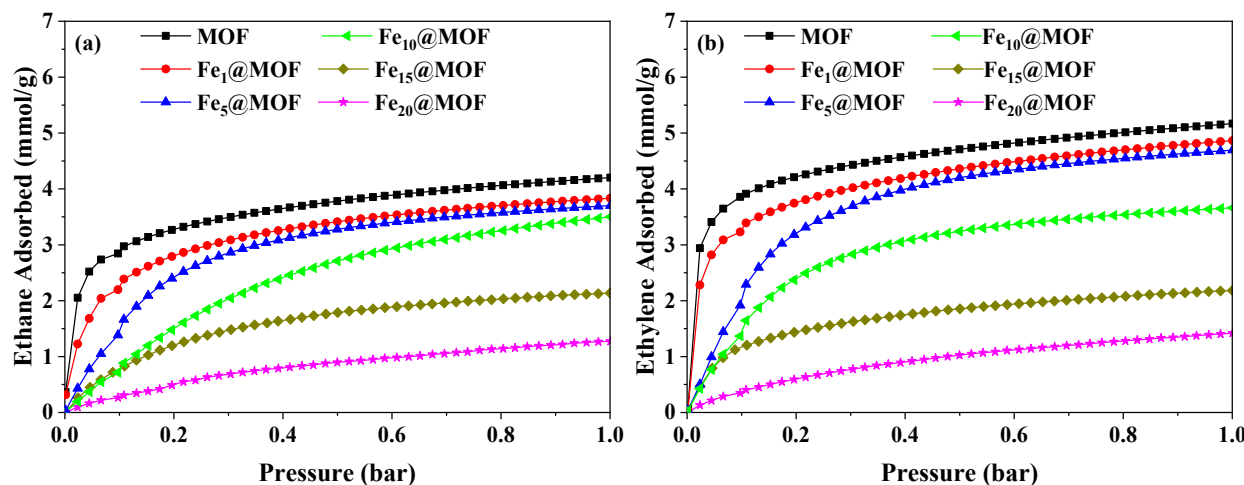ectively. Field-emission scanning electron microscopy (FE-SEM, Hitachi model S4700) and high-resolution transmission electron microscopy (HR-TEM) images were used to assess the structural morphology of the designed composites. Before taking images, the samples were dispersed in methanol and sonicated for 15 min. Then, the samples were collected using copper grids covered with carbon film. The magnetic properties of the Fe_x@MOF composites were characterized by electron paramagnetic resonance (EPR) Bruker instrument. All the samples were exposed to a magnetic field in the range of 50–550 mT, and the EPR spectra were recorded. Thermogravimetric analysis (TGA) was used to determine the thermal stability of the Fe_2O_3, bare MOF, and Fe_x@MOF using a Q500 TAInstrument. The temperature was varied from 25 to 550 °C at a temperature ramp of 25 °C/min under the flow of N_2 at 40 mL/min.

2.5. Adsorption isotherm measurements

The unary C_2H_6 and C_2H_4 adsorption isotherms were measured at 25 °C over the pressure range of 0–1 bar using a volumetric gas analyzer (Micromeritics, 3Flex). Prior to each test, MOF, Fe_1@MOF, Fe_5@MOF, Fe_{10}@MOF, Fe_{15}@MOF, and Fe_{20}@MOF were degassed on a Micromeritics Smart VacPrep instrument under vacuum at 120 °C for 5 h to remove any preadsorbed moisture or gases. The equilibrium adsorption isotherms were fitted using three different adsorption models (Fig. S1 and Table S1-S3), namely Freundlich, Langmuir, and Sips to describe the adsorption process over the synthesized composite sorbents, as described in Eqs. S1-S3, Supporting Information.

2.6. Magnetic induction breakthrough experiments

The dynamic adsorption–desorption experiments under magnetic induction heating were carried out in an in-house lab setup, as schematically depicted in Fig. 2. As metallic columns tend to heat up under induction heating, a quartz tube with inner diameter of 1 cm and a length of 8 cm was used for the adsorption–desorption experiments instead. The fittings and connectors for the inlet and outlet openings of the column were chosen from nonconductive plastic materials. The adsorption step was carried out at 25 °C and 1 bar, followed by desorption during which the sorbents were exposed to a magnetic field using an induction heating system (EASYHEAT 1.2 to 2.4 kW-AMBRELL) equipped with an induction coil 4 cm in length, 2.5 cm in diameter, and with 8 turns. A fiber-optic (FO) temperature sensor (OPTOCON, TS3-

10MM-02) was installed in such a way that the tip of the sensor can touch the sorbent bed from inside to ensure accurate temperature measurement. The temperature profiles at different magnetic fields for each experiment were recorded using a temperature controller (FOTEMP4-PLUS-P0-V-B). To minimize the heat loss to the surroundings, a specially designed shield (Faraday cage) made from low conductive steel was attached to the in-house setup and placed in the center of the induction coil. Prior to each experiment, the sorbent was *in-situ* activated at 125 °C for 5 h under 20 mL/min Ar flow . Next, the column was cooled down to 25 °C and a gas feed with composition of 50/50 mol% C_2H_4/C_2H_6 and flow rate of 50 mL/min was fed into the bed simultaneously with 5 mL/min Ar. Mass flow controllers (MFCs) were used to control the gas flow rates, and the outlet gas flow was analyzed by a mass spectrometer (MKS). When the bed was saturated with C_2H_6 and C_2H_4, the inlet feed was switched to Ar at 20 mL/min, while turning the magnetic field on at different strengths (12.6, 21.4, 31.4 mT). The desorption was continued until the concentrations of C_2H_6 and C_2H_4 reached zero at the column outlet.

2.7. Specific heat absorption rate measurements

The specific heat absorption rate (*SAR*, W/g) during desorption step was calculated by (Eq. S5). The composite sorbents with varied Fe_2O_3 loadings (Fe_1, Fe_5, Fe_{10}, Fe_{15}, Fe_{20}) were dispersed in water using a glass vial and exposed to three different magnetic fields, while the temperature gradients were recorded online, as shown in Fig. S2. The estimated SAR values are summarized in Table S4-S6.

3. Results and discussion

3.1. Characterization of Fe_x@MOF composites

The N_2 physisorption isotherms and PSD profiles of the bare MOF and Fe_x@MOF composites are shown in Fig. 3, and the corresponding textural properties are provided in Table 1. The N_2 isotherms and PSD profile of the bare Fe_2O_3 are also presented in Fig. S3, Supporting Information. The Fe_2O_3 displayed Type II isotherms, characteristic of its nonporous nature. On the other hand, the bare MOF displayed Type I isotherms with a narrow hysteresis loop (Type IV), indicative of its predominant microporous structure with some degree of mesoporosity (Fig. 3a). The PSD profiles in Fig. 3b confirmed the presence of both micro- and small mesopores in the range of 2–5 nm for this material. For magnetic composites, N_2 uptake was reduced with increasing Fe_2O_3 loading, with Fe_1@MOF displaying slightly lower and Fe_{20}@MOF much lower N_2 uptake relative to the bare MOF. This physisorption behavior
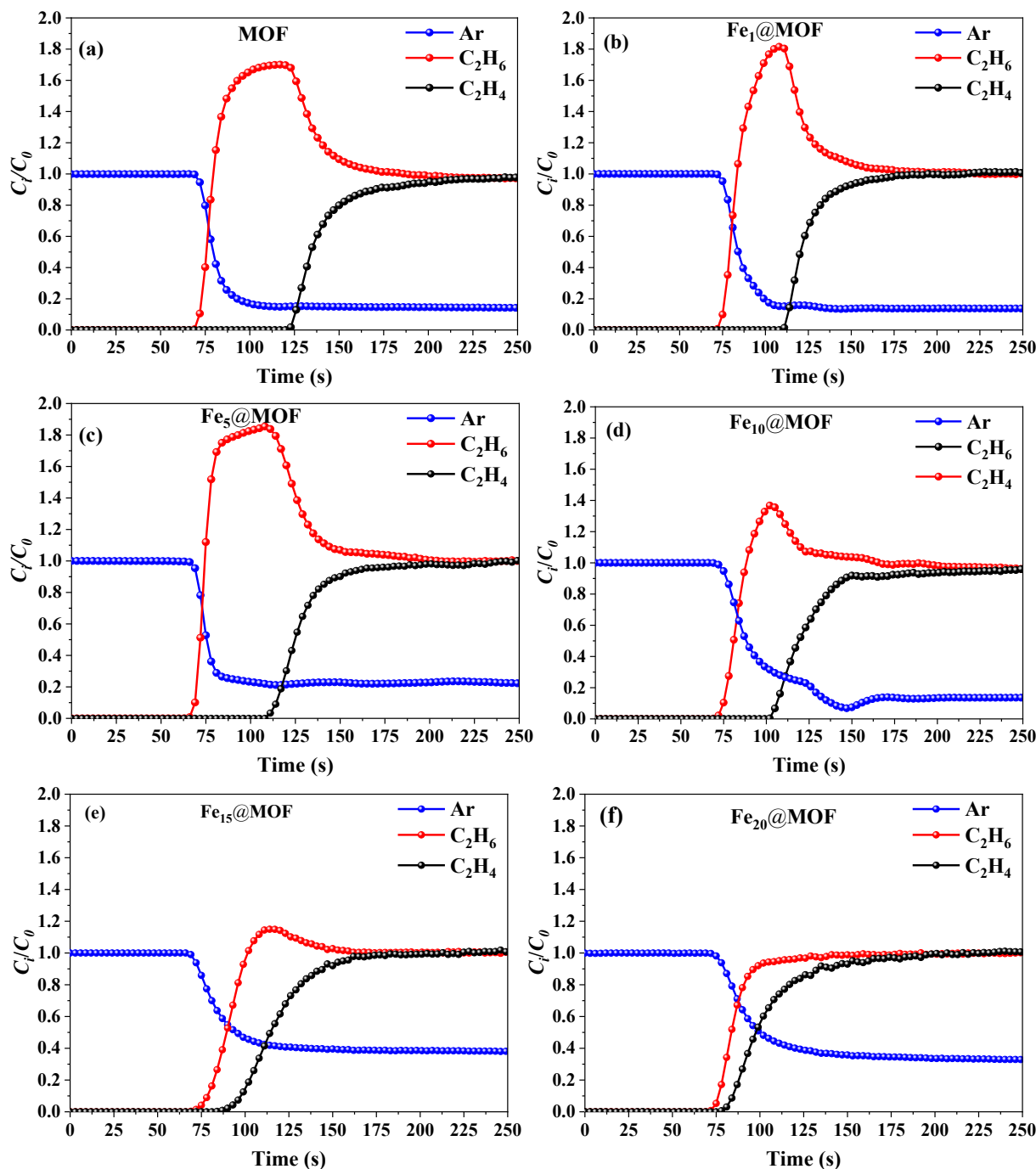
Fig. 7. Dynamic concentration profiles for 50/50 vol% C_2H_6/C_2H_4 at 25 °C and 1 bar over (a) MOF, (b) $Fe_1@MOF$, (c) $Fe_5@MOF$, (d) $Fe_{10}@MOF$, (e) $Fe_{15}@MOF$, and (f) $Fe_{20}@MOF$.

could be attributed to the loss in the microporosity character of the MOF in magnetic sorbents due to increasing the content of Fe_x. However, the hybridized isotherms of Type I-IV were still observed for these materials, indicating that the MOF crystals grown on the surface of the magnetic particles were still microporous, which is desirable to maintain high adsorption capability for these core–shell composites. This physisorption behavior agrees well with the literature reports on other MOF-based composites synthesized by this approach [25]. For example, in the study reported by Sadiq et al., [23] the surface area and pore volume were reduced for the UiO-66@MgFe$_2$O$_4$ composites relative to the bare UiO-66. Increasing the amount of Fe_x to 15 and 20 wt%, as in $Fe_{15}@MOF$ and $Fe_{20}@MOF$, resulted in a dramatic reduction in microporosity,

albeit the sorbents retained their mesoporous nature (Table 1). The reduction in microporosity of the $Fe_{15}@MOF$ and $Fe_{20}@MOF$ is returned to the nonporous nature of Fe_2O_3 (Fig. S3), as evidenced by almost negligible N_2 uptake over this material. The agglomeration of the crystals during the synthesis could likely be another reason for reduced porosity in these samples.

From Table 1, the BET surface area and micropore volume (V_{micro}) of the bare MOF were estimated to be 1207 m^2/g and 0.41 cm^3/g, respectively, whereas for $Fe_{10}@MOF$, these values were reduced by 27 % (ca. 877 m^2/g) and 44 % (ca. 0.23 cm^3/g), respectively. On the contrary, the mesopore volume (V_{meso}) slightly enhanced from 0.15 to 0.16 cm^3/g for this material. This could likely be attributed to the

Table 3
Dynamic adsorption data for binary runs at 25 °C and 1 bar for the MOF and the corresponding Fe_x@MOF composites.

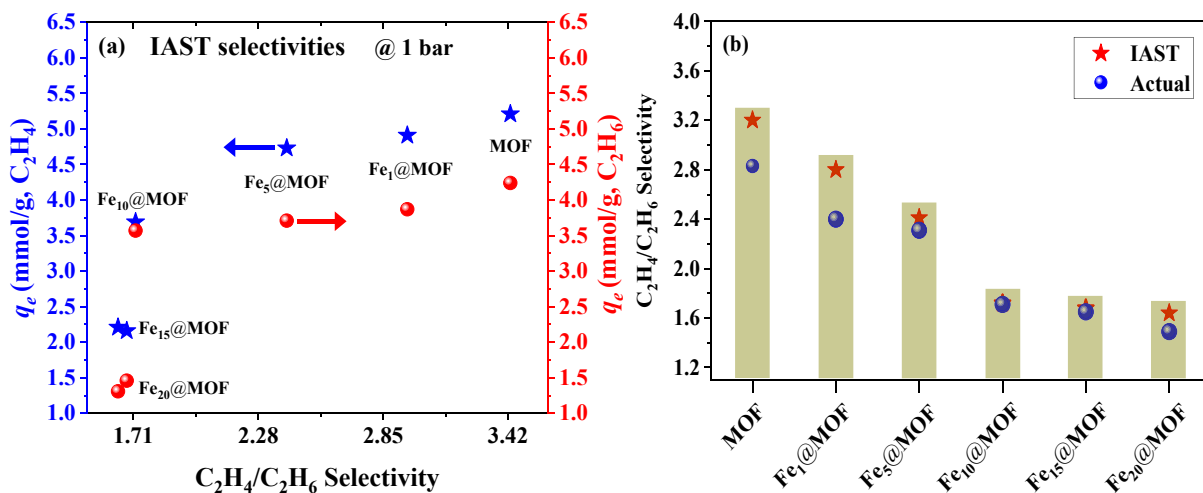| Breakthrough parameter	$t_{ads,5\%}$ (s)	$t_{ads,50\%}$ (s)	$t_{ads,95\%}$ (s)	Breakthrough width (s)	$q_{ads,5\%}$ (mmol/g)	$q_{ads,50\%}$ (mmol/g)	$q_{ads,95\%}$ (mmol/g)
C_2H_6							
MOF	70	80	94	24	0.23	0.89	1.07
Fe_1@MOF	74	82	98	24	0.24	0.91	1.10
Fe_5@MOF	68	73	91	23	0.22	0.83	1.06
Fe_{10}@MOF	73	82	97	24	0.20	0.80	1.10
Fe_{15}@MOF	73	92	101	28	0.19	0.73	0.92
Fe_{20}@MOF	73	82	103	30	0.18	0.64	0.90
C_2H_4							
MOF	124	133	189	65	1.40	2.16	3.02
Fe_1@MOF	113	124	161	48	1.29	1.86	2.64
Fe_5@MOF	112	122	159	47	1.04	1.79	2.26
Fe_{10}@MOF	106	118	147	41	0.84	1.38	1.88
Fe_{15}@MOF	92	114	131	39	0.79	1.15	1.52
Fe_{20}@MOF	88	97	126	38	0.70	1.00	1.35

Fig. 8. (a) IAST selectivity versus equilibrium adsorption capacity (mmol/g) of C_2H_6 and C_2H_4 obtained for MOF and corresponding Fe_x@MOF composites at 25 °C and 1 bar, and (b) comparison between the IAST and actual C_2H_4/C_2H_6 selectivities.

formation of MOF crystals with defects or formation of additional mesopores at the interface of Fe_2O_3 and the MOF crystals. In conclusion, these results highlight that adding low concentration of Fe_2O_3 into the MOF's solvothermal solution (e.g., Fe_1, Fe_5, Fe_{10}) can generate hybrid sorbents within which MOF constituent still retains its micro– and mesoporosity, in agreement with previously reported data in the literature [27–30]. However, exceeding these amounts can dramatically deteriorate its porosity.

The surface morphology of the synthesized sorbents was investigated by SEM and TEM analyses. The SEM image in Fig. 4a shows the well-intergrown aggregates of MOF polyhedral crystals formed on separate Fe_2O_3 particles in the Fe_1@MOF sorbent, confirming the formation of core–shell material.[23,31] The composite structure of Fe_1@MOF could also be confirmed by the TEM image shown in Fig. 4b. The magnetic sorbent consisted of bulk Fe_2O_3 dark region and sparse crystals of MOF (light region) as the grown crystals on the Fe_2O_3 surface. A similar morphological characteristic was observed for the other Fe_x@MOF composites, thus their corresponding images were not included here.

The elemental composition of Fe_1@MOF at one of the aggregated particles of Fe_2O_3 covered with MOF crystals (shown by the yellow circle) was determined by EDX mapping analysis. The images in Fig. 4c-e confirm the formation of magnetic composites consisting of Ni, as the metal representing the MOF constituent, and Fe as the magnetic element in the Fe_2O_3 constituent. The EDX analysis also confirmed that Fe_2O_3 particles were concentrated at the center of the composite bulk (Fig. 4e),

whereas the MOF crystals were concentrated close to the edge of the particle (Fig. 4c-d). It should be pointed out here that the composition of Fe determined from EDX data was relatively small, whereas Ni composition was estimated to be high (Table S7). Given that EDX analysis provides insight on the surface composition, the low concentration of Fe could be ascribed to the thick film of MOF crystals covering the Fe_2O_3 particles, as evidenced from Fig. 4a. Overall, these characterization results qualitatively confirm the successful formation of magnetic composites with core–shell structure.

The TGA profiles of the Fe_2O_3, the bare MOF, and the corresponding composites are presented in Fig. 5a. The initial weight loss observed in the temperature range up to 375 °C for the bare MOF and the composites was due to the physically adsorbed moisture [25], however, the Fe_2O_3 was retained its thermal stability over this range of temperature. As the temperature increased to above 375 °C, much larger weight loss was observed, which was associated with the organic linker elimination and the MOF deterioration. The magnetic composites displayed weight losses intermediate between the Fe_2O_3 and the bare MOF. Upon increasing the Fe_2O_3 loading, the thermal stability of the composites increased substantially. For example, Fe_{20}@MOF exhibited ~16 % thermal stability improvement relative to the bare MOF, whereas the TGA profile of the Fe_1@MOF with the highest MOF loading approached that of the bare MOF. It can be concluded from the TGA data that Fe_2O_3 enhanced the thermal stability of the composite sorbents, which is desirable for improving the magnetization capability, and hence standing high
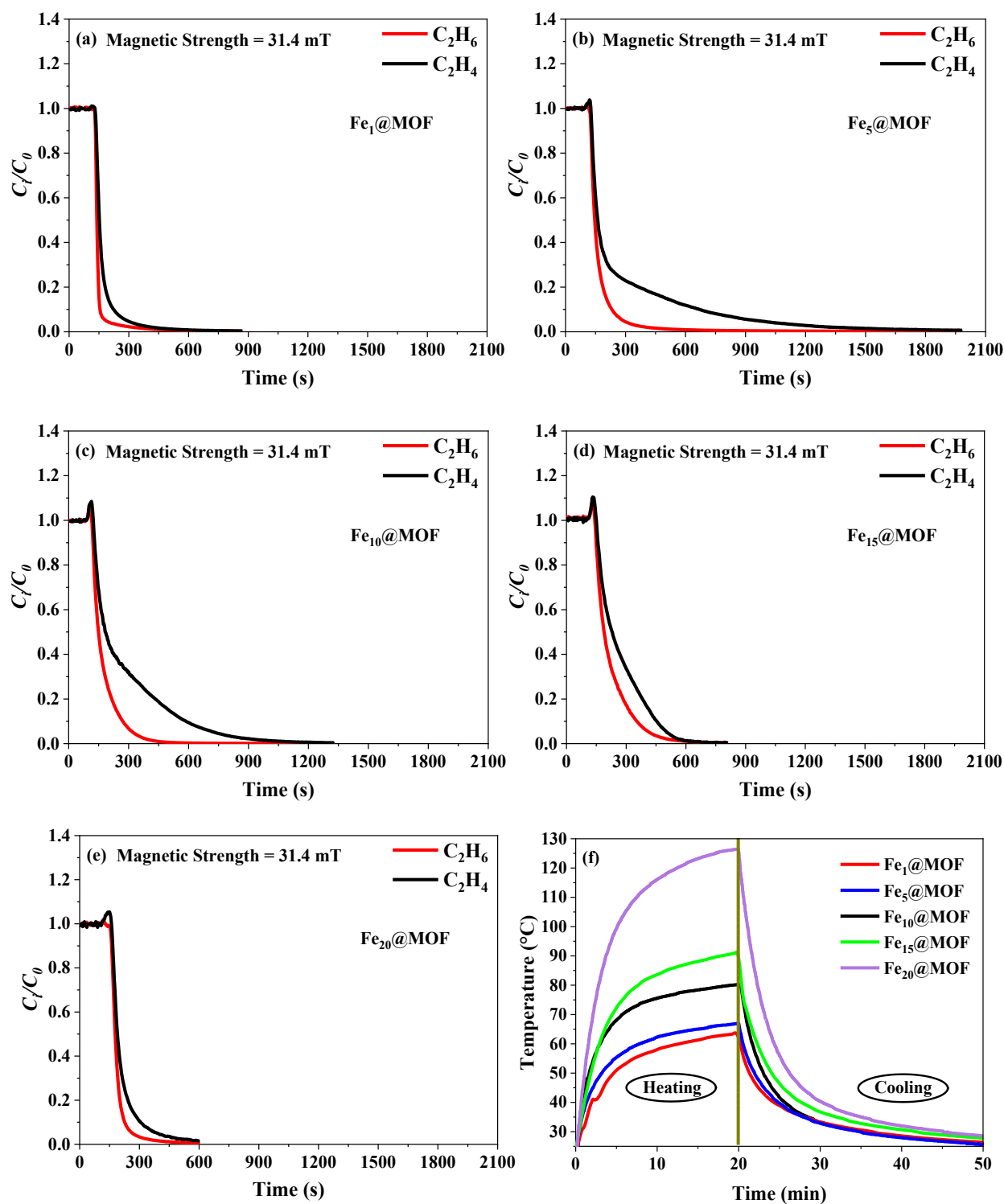
Fig. 9. Desorption profiles of C_2H_6 and C_2H_4 at 31.4 mT over (a) $Fe_1@MOF$, (b) $Fe_5@MOF$, (c) $Fe_{10}@MOF$, (d) $Fe_{15}@MOF$, and (e) $Fe_{20}@MOF$; and (f) temperature profiles during desorption and cooling steps.

desorption temperatures.

Electron paramagnetic resonance analysis was also performed to investigate the sorbents' magnetism ability and the results are shown in Fig. 5b. As can be seen, increasing the Fe_2O_3 loading from 1 to 20 wt% gave rise to increased EPR spectrum intensity with $Fe_{20}@MOF$ absorbing the highest amount of heat upon exposure to the magnetic field. It was also noted that the heat absorption rate is a strong function of Fe_x loading. Therefore, the SAR values were calculated for magnetic

composites with varied Fe_2O_3 by Eq. S5, following a method reported in the literature [23] and the obtained results are summarized in Table 2. The temperature gradient profiles from the SAR experiments are also shown in Fig. S2. As expected, increasing the magnetic field from 21.6 to 31.4 mT resulted in > 80 % increment in the specific heat absorption for the same magnetic (Fe_x) content. For example, at 21.6 mT the SAR was increased from 1.86, 3.69, 4.21, 4.94, and 9.2 W/g to 24.45, 30.02, 32.86, 37.59, and 60.27 W/g at 31.4 mT for Fe_1, Fe_5, Fe_{10}, Fe_{15}, and

Table 4

Dynamic desorption data for binary runs at 31.4 mT and 1 bar over Fe$_x$@MOF composites.

Sorbent	$t_{des, (C_2H_6)}$ (s)	$t_{des, (C_2H_4)}$ (s)	Desorption rate (r_{des}), C$_2$H$_6$ (mmol/g.min)	Desorption rate (r_{des}), C$_2$H$_4$ (mmol/g.min)	Cooling rate (°C/min)
Fe$_1$@MOF	350	350	0.012	0.018	15.5
Fe$_5$@MOF	600	1400	0.015	0.020	13.2
Fe$_{10}$@MOF	500	950	0.021	0.025	13.1
Fe$_{15}$@MOF	550	550	0.017	0.023	12.0
Fe$_{20}$@MOF	400	500	0.016	0.019	11.3
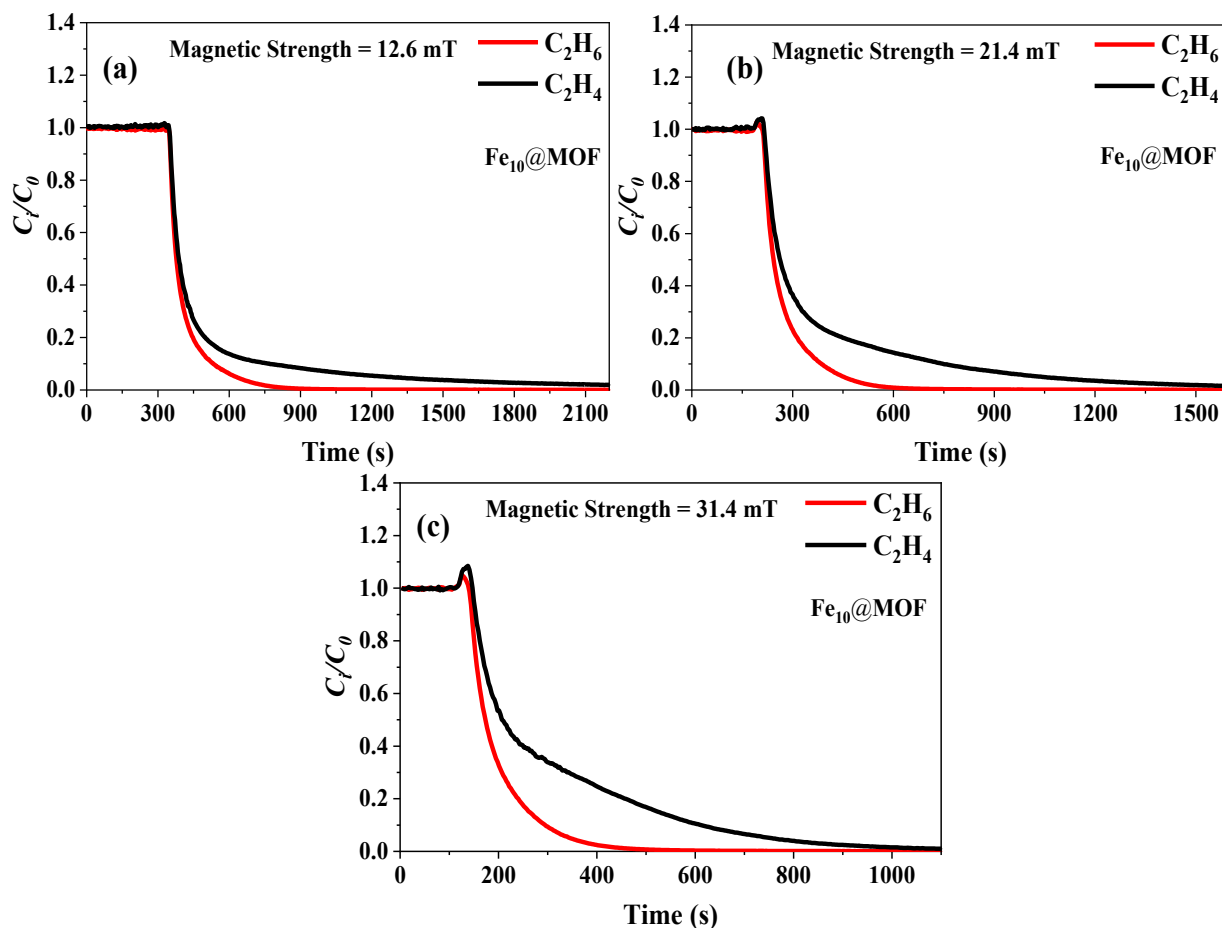
Fig. 10. Desorption profiles of C$_2$H$_6$ and C$_2$H$_4$ at (a) 12.6, (b) 21.4, and (c) 31.4 mT field strength over Fe$_{10}$@MOF.

Fe$_{20}$, respectively. On the other hand, comparing the SAR values at constant magnetic field (e.g., 31.4 mT) for different magnetic compositions, the SAR was increased by ~60 % for Fe$_{20}$ compared to Fe$_1$, in agreement with the EPR data in Fig. 5b. As this figure demonstrates, the intensity of the EPR spectrum was the highest for Fe$_{20}$@MOF across the entire magnetic field, and decreased as the amount of Fe$_2$O$_3$ in the composite decreased. The high SAR of the composite makes it suitable as a magnetic responsive sorbent, which can be regenerated upon exposure to an external magnetic field, as will be discussed in the following sections.

3.2. Unary C$_2$H$_6$ and C$_2$H$_4$ adsorption isotherms

The equilibrium adsorption isotherms of ethane and ethylene obtained at 25 °C are presented in Fig. 6a-b. Like the parent MOF, the magnetic composites exhibited slightly higher affinity toward ethylene over ethane. Notably, the shape of the isotherms resembled that of the isotherms over the prsitine MOF, displaying a steep increase at low pressures followed by a gradual increase in the uptake at higher pressures. However, the sharpness of the isotherms and the amount of ethane/ethylene adsorbed reduced as the Fe$_2$O$_3$ content in the Fe$_x$@MOF composites increased. In particular, significant reductions in equilibrium uptake of both species were observed for Fe$_{15}$@MOF and Fe$_{20}$@MOF.

Generally, the reduction in ethane and ethylene equilibrium capacities and the change in isotherms shape with increasing the composition of Fe$_x$ could be attributed to the reduction in surface area and porosity of the composites, as discussed earlier. Such decreasing trend in equilibrium gas uptake with increased metal loading has also been reported for the other MOF-based composites [27–29]. The bare MOF displayed an equilibrium capacity of 4.24 mmol/g for ethane and 5.21 mmol/g for ethylene at 1 bar, whereas Fe$_1$@MOF, Fe$_5$@MOF, Fe$_{10}$@MOF, Fe$_{15}$@MOF, and Fe$_{20}$@MOF achieved capacities of 3.86, 3.73, and 3.57, 2.16, respectively for ethane and 4.91, 4.73, 3.69, 2.21, and 1.46 mmol/g, respectively for ethylene, as shown in Fig. 6a and 6b.

The measured adsorption data were also fitted with three different adsorption models (Langmuir, Freundlich, Sips) to determine the best model that describes the isotherms, and to estimate the IAST selectivities

Table 5
Dynamic desorption data for binary runs at 12.6, 21.4, and 31.4 mT over Fe$_x$@MOF composites.

Sorbent	$t_{des, (C_2H_6)}$ (s)	$t_{des, (C_2H_4)}$ (s)	Desorption rate (r_{des}), C$_2$H$_6$ (mmol/g.min)	Desorption rate (r_{des}), C$_2$H$_4$ (mmol/g.min)
@ 12.6 mT				
Fe$_{10}$@MOF	900	2100	0.012	0.011
Fe$_{15}$@MOF	1200	1200	0.011	0.010
Fe$_{20}$@MOF	600	550	0.009	0.008
@ 21.4 mT				
Fe$_{10}$@MOF	600	1500	0.018	0.016
Fe$_{15}$@MOF	900	1100	0.014	0.014
Fe$_{20}$@MOF	7z50	600	0.011	0.011
@ 31.4 mT				
Fe$_{10}$@MOF	500	950	0.021	0.025
Fe$_{15}$@MOF	550	550	0.017	0.023
Fe$_{20}$@MOF	400	500	0.016	0.019

from the adsorption isotherms. As illustrated in Fig. S1, Sips model was found to satisfactorily describe the ethane and ethylene uptakes as compared with Langmuir and Freundlich models; thus, Sips model was selected for estimation of the IAST selectivity values. The parameters of the isotherm models are reported in Table S1-S3, Supporting Information. The comparison of ideal (IAST) and actual selectivity values are discussed in the following section.

3.3. Magnetic induction breakthrough experiments

To assess the separation capability of the magnetic sorbents, breakthrough experiments were carried out using a binary gas mixture with equimolar concentration of C$_2$H$_4$ and C$_2$H$_6$. As a control experiment, pristine MOF was also tested under the same conditions, and the dynamic concentration profiles are shown in Fig. 7. In agreement with their MOF parent, the magnetic sorbents all exhibited preferential adsorption of ethylene over ethane with high separation efficiency, as evident from the profiles. Looking at the concentration fronts, the breakthrough of ethylene from the bed outlet caused an overshoot in the wavefront of ethane, whose magnitude was significant for the bare MOF but decreased as the Fe$_2$O$_3$ content increased to 15 wt%, and eventually disappeared for Fe$_{20}$@MOF (see Fig. 7a-f). The presence of the overshoot above the relative concentration of $C_i/C_0 = 1$ stems from the displacement of weaker adsorbed ethane molecules by the strongly adsorbed ethylene molecules during adsorption step. When ethylene approaches the end of the column, binary equilibrium is attained and the mole fractions of both gases are returned to their feed compositions [32,33]. Since the uptake of ethane was generally lower over Fe$_{15}$@MOF and Fe$_{20}$@MOF than over other materials, the overshoot was not observable (or negligible) in the desorption profile of ethane [34–37]. It was also noted that the difference in breakthrough time ($t_{ads,5\%}$) for ethane and ethylene decreases on the order of MOF > Fe$_1$@MOF > Fe$_5$@MOF > Fe$_{10}$@MOF > Fe$_{15}$@MOF > Fe$_{20}$@MOF, as also evident from Table 3. Notably, the ethane dynamic capacity at $t_{ads95\%}$ was much lower than its equilibrium capacity which may be attributed to the competitive adsorption of ethane and ethylene over these materials. Moreover, comparison of the breakthrough widths revealed no significant changes in the shape of the fronts. But as mentioned earlier, Fe$_2$O$_3$ is a nonporous material and increasing its composition leads to microporosity reduction, resulting in a gradual decline in ethylene uptake and the breakthrough width.

The C$_2$H$_4$/C$_2$H$_6$ selectivities estimated from the IAST model are shown in Fig. 8a as a function of the equilibrium capacities (q_e). It is clear that these magnetic composites are ethylene-selective similar to the pristine MOF, due to strong π-complexation interactions between

ethylene's unsaturated double bond and the MOF's open metal sites [38]. However, the selectivity showed a decreasing trend with increased Fe$_2$O$_3$ content. For example, while the C$_2$H$_4$/C$_2$H$_6$ selectivity of the bare MOF was 3.20, it was reduced to 1.64 for Fe$_{20}$@MOF. The controlled factors for achieving high ethylene selectivity appears to be high surface area and microporosity with more preferential sites for ethylene adsorption. As long as the sorbent retains its high surface area and microporosity, the C$_2$H$_4$/C$_2$H$_6$ selectivity will be high, in agreement with the parent MOF. The data reported in Table 3 are consistent with the literature [38,39]. The comparison of C$_2$H$_4$/C$_2$H$_6$ selectivities estimated from the IAST model and the breakthrough profiles (actual) is demonstrated in Fig. 8b. The difference in the estimated selectivity values from the model and actual experiments was as high as ~10 %, indicating a relatively good match between the theoretical and actual selectivities. However, it is worth noting here that the difference in the estimated values was more apparent for the bare MOF and Fe$_1$@MOF compared to other samples.[38] This was further supported by the separation efficiency ($\alpha_{C_2H_4/C_2H_6}$) values as a function of magnetic composition, which were estimated from the $q_{ads,5\%}$ using eq. S4, and the results are shown in Fig. S4. The separation efficiencies of the bare MOF and Fe$_1$@MOF were found to be the highest, in accordance with their highest surface area and micropore volume [40].

The desorption profiles of ethane and ethylene along with the temperature profiles (heating and cooling) as a function of time are depicted in Fig. 9a-f. To evaluate the effect of Fe$_x$ content on the ethane and ethylene desorption rates, desorption experiments were performed at a fixed magnetic field strength (31.4 mT). Heating the composites via exposure to magnetic field resulted in the bed temperature rise (ΔT) but its magnitude varied across the composites (Fig. 9f). As shown in this figure, the higher content of Fe$_x$ led to a higher ΔT under fixed magnetic field intensity, with Fe$_1$@MOF displaying the lowest ΔT (40 °C) and Fe$_{20}$@MOF displaying the highest ΔT (100 °C). On the basis of the SAR results, such trend was expected mainly because the heat absorption increased with increasing the magnetic particles loading, where the Fe$_{20}$ exhibited the highest specific heat absorption rate, which caused the bed temperature to rise dramatically.

The different responses to magnetic field during desorption step resulted in varied desorption rates for both ethane and ethylene, the extent of which depended primarily on the content of Fe$_x$. There was no apparent difference in the desorption profiles for the composites, however, the desorption rates were found to be slightly different across the samples. In Fe$_1$@MOF, Fe$_5$@MOF, and Fe$_{10}$@MOF, a gradual increase in the outlet mole fraction of gases was observed, whereas in the case of Fe$_{15}$@MOF and Fe$_{20}$@MOF, a decline in the outlet mole fraction was noted (Fig. 9a-e). It is worth noting here that although the desorption times were different for the composites, a fixed time interval (0–350 s for ethane desorption and 0–500 s for ethylene desorption) was considered in the estimation of rates, and the data are summarized in Table 4. The desorption rates of ethylene were increased from 0.018 for Fe$_1$@MOF to 0.020 and 0.025 mmol/g.min for Fe$_5$@MOF and Fe$_{10}$@MOF, respectively, then reduced to 0.023 and 0.019 mmol/g.min for Fe$_{15}$@MOF and Fe$_{20}$@MOF, respectively. Notably, the desorption rate was fastest over Fe$_{10}$@MOF (0.025 mmol/g.min) mainly because of the combination of high energy absorption and low ethylene uptake. The desorption time, gas uptake, and the energy absorption of sorbent are the main factors affecting the desorption rate in induction heating. Part of the energy absorbed is consumed by the desorption enthalpy, some of it warms the sorbent, and the rest is dissipated in the gas stream [19,24]. As the heat intensity increased with Fe$_x$, a higher portion of the energy was absorbed to warm the bed as the MOF had a low thermal conductivity [23]. Similar trend was observed for ethane but with lower desorption rate because ethylene was the selective gas in these sorbents. The cooling rates for the composites were recorded as well, and as expected, the cooling rate became slower (Table 4) as the desorption temperature was higher due to a longer time required to cool down the bed back to the room temperature.
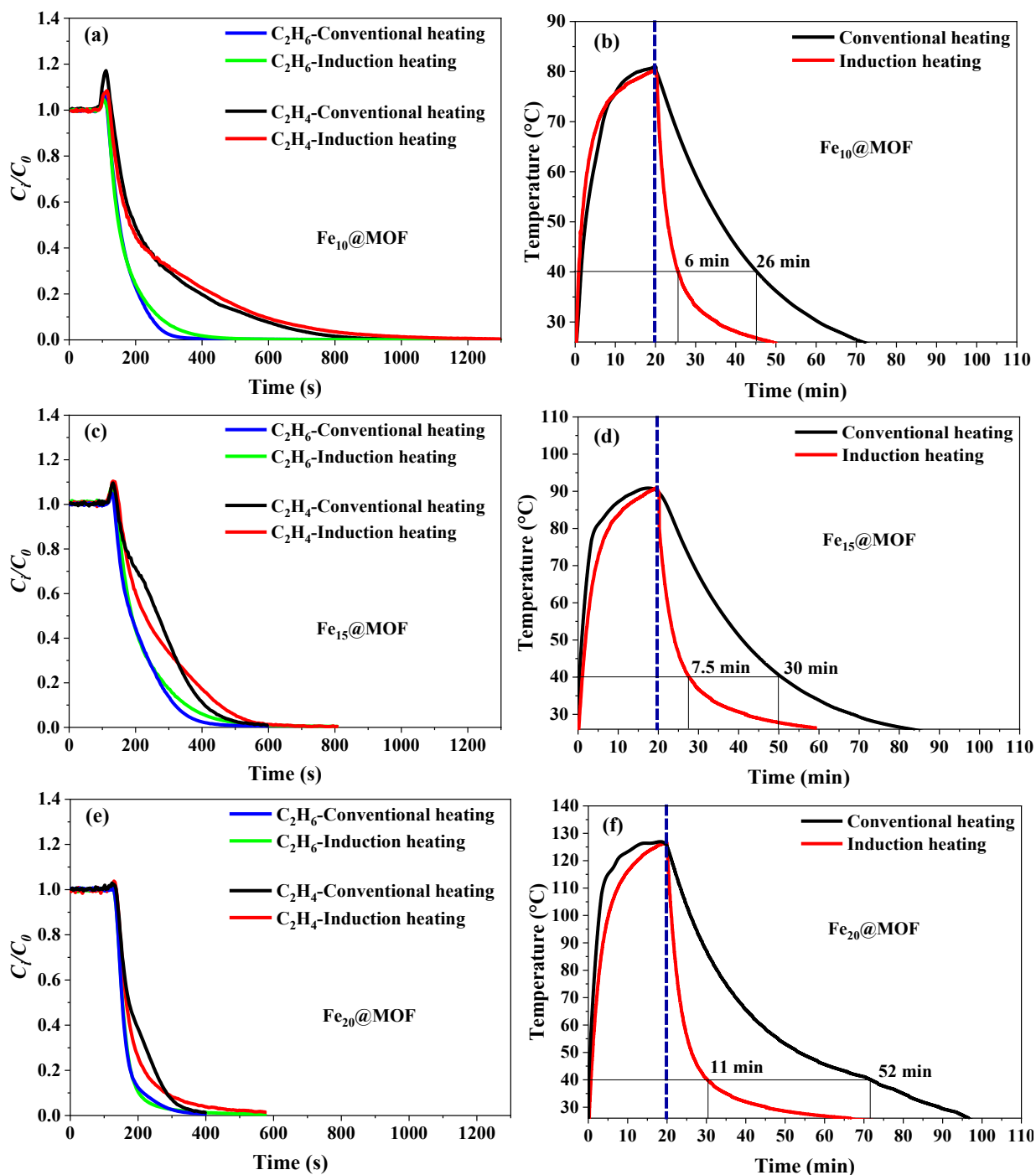
Fig. 11. Comparison between conventional and induction heating and their effect on desorption and cooling rates (a-b) $Fe_{10}@MOF$, (c-d) $Fe_{15}@MOF$, and (e-f) $Fe_{20}@MOF$.

Table 6
Comparison between conventional and induction heating and their effect on desorption and cooling rates.

Sorbent	$t_{des, (C_2H_6)}$ (s)	$t_{des, (C_2H_4)}$ (s)	Desorption rate (r_{des}), C_2H_6 (mmol/g.min)	Desorption rate (r_{des}), C_2H_4 (mmol/g.min)	Cooling rate (°C/min)
$Fe_{10}@MOF$-induction	500	950	0.021	0.025	13.1
$Fe_{10}@MOF$-conventional	400	900	0.022	0.025	3.1
$Fe_{15}@MOF$-induction	550	550	0.018	0.023	12.0
$Fe_{15}@MOF$-conventional	480	550	0.017	0.023	3.0
$Fe_{20}@MOF$-induction	400	500	0.016	0.019	11.3
$Fe_{20}@MOF$-conventional	390	400	0.017	0.020	2.4

3.4. Effect of magnetic field strength

To evaluate the effect of magnetic field strength, desorption profiles were collected at three different field intensities (12.6, 21.4, 31.4 mT) for each of the magnetic composites, as shown in Fig. 10a-c (for Fe_{10}@MOF) and Fig. S5. As the data in Table 5 suggest, increasing the magnetic field strength from 12.6 to 31.4 mT gave rise to higher ethane/ethylene desorption rates for all sorbents. For instance, the desorption rate of ethylene over Fe_{10}@MOF increased from 0.011 mmol/g.min to 0.016 and 0.025 mmol/g.min, when field intensity increased from 12.6 to 21.4 and 31.4 mT, respectively. It can be deduced that with high magnetic particles content (Fe_x), the energy absorption is mostly consumed in warming the adsorption bed which causes the sorbent temperature to increase, leading to a higher desorption rate. Similar enhancement in desorption rate was observed for Fe_{15}@MOF and Fe_{20}@MOF, albeit the enhancement was the highest for Fe_{20}@MOF (at 58 % vs 56 % for Fe_{10}@MOF and Fe_{15}@MOF). Moreover, ethane desorption rate was lower than that of ethylene in all cases due to the higher ethylene uptake relative to ethane. For example, for Fe_{10}@MOF, the desorption rate enhancement with field intensity was 56 % for ethylene, whereas it was 42 % for ethane.

3.5. Comparison between conventional and induction heating

To assess the effectiveness of induction heating, the desorption experiments were also conducted under conventional heating at three different temperatures (80, 90, 125 °C) in order to compare with those conducted under different magnetic field strengths (12.6, 21.4, 31.4 mT). The corresponding results are illustrated in Fig. 11a-f and the experimental data are summarized in Table 6. At first glance, there was no noticeable differences in the concentration profiles under both induction and conventional heating modes. Similarly, the desorption rates of ethane and ethylene were roughly identical in both cases. This can be ascribed to the sorbent mass and the smaller diameter of the adsorption column that did not show the real desorption performance under a magnetic field, as the distance between the central spot of sorbent and the wall of column is very close. As the distance between the column and the central spot of sorbent was very close, the heating transfer was faster, and thus the heat generated from both methods gave rise to similar desorption performances. The heating mechanism in the conventional method is essentially depended on the heat transfer between the column wall and the sorbent, whereas the induction heating is an indirect heating via magnetic wave penetration due to the secondary magnetic field creation between the magnetic particles in the sorbent and the current inside the induction coil [19].

On the contrary, the advantage of indirect induction heating over the conventional method was manifested in the cooling step where a much faster rate (~76 %) was obtained, as shown in Fig. 11(b, d, f). During thermal desorption, almost the entire column is heated, resulting in a long cooling time, whereas in the induction heating, the heating is concentrated within the length of induction coil and the adsorption column, hence the cooling rate is faster. The cooling rates – under the conventional heating mode – were 3.1, 3.0, and 2.4 °C/min for Fe_{10}@MOF, Fe_{15}@MOF and Fe_{20}@MOF, respectively, which increased to 13.1, 12.0, and 11.3 °C/min when induction heating was used. Faster cooling rate is advantageous from a process point of view where the cooling step is usually the limiting step, making the cycle time long in conventional TSA processes. This significant increase in cooling rates makes the induction heating a promising regeneration method for adsorptive separation of paraffins and olefins.

Table S8 provides a comparison between the SAR values and the desorption rates obtained from this study and those reported in the literature. Our core–shell magnetic composites displayed comparable performance to those reported in the literature for magnetic-induced CO_2 desorption from magnetic sorbents. For example, Fe_{20}@MOF exhibited higher SAR than $MgFe_2O_4$@UiO-66 at comparable magnetic

strength of ~32 mT (60.27 vs 46.7 W/g). However, at lower magnetic compositions (e.g., Fe_{10}@MOF), SAR was noted to be lower than for $MgFe_2O_4$@UiO-66. Furthermore, it was noted that SAR was much lower than what was reported for 113X-(20/10 wt%) Fe_3O_4. The difference may be attributed to the content of magnetic particles, as the nominal Fe_x amounts used were estimated with respect to the metal (Ni) amount in the MOF not to the entire mass of the MOF. This means that the actual amount of Fe_2O_3 in Fe_{20}@MOF might be lower than the 10 wt% Fe_3O_4 in 13X-(20/10 wt%) Fe_3O_4. Besides, this discrepancy might also stem from different degrees of ferromagnetism of Fe_2O_3 and Fe_3O_4.

4. Conclusions

In this study, five magnetic composites with varied composition and core–shell structure were developed and assessed for ethylene/ethane separation via induction heating. The specific heat absorption rate measurements indicated that the generated heat upon exposure to magnetic field during desorption is a direct function of Fe_x content and the magnetic field strength. Our results indicated the trade-offs between enhanced heating efficiency and reduced capture capacity for the Fe_x@MOF composite sorbents, in that while the higher Fe_x loading enhanced the responsiveness of the sorbent to the magnetic field, it reduced the ethylene/ethane capture capacities. This implies that in the design and development of stimuli-responsive sorbents, it is essential to address such trade-offs in order to maximize the separation efficiency. The dynamic desorption experiments revealed that while increasing magnetic field strength can enhance desorption rates, increasing the Fe_x loading at constant magnetic field strength results in reduced desorption rates. Furthermore, comparison between conventional and induction heating methods in regeneration of sorbents showed that despite similar desorption performances, the induction heating is far superior to the conventional heating in terms of enhanced cooling rates, and hence shorter cycle time. Shortening cooling step can dramatically reduce the cycle step for swing adsorption processes, thereby improving the system throughput and reducing the column size. The findings of this proof-of-concept study highlight the potential of magnetic composites as stimuli-responsive sorbents for separation of paraffins/olefins.

Declaration of Competing Interest

The authors declare that they have no known competing financial interests or personal relationships that could have appeared to influence the work reported in this paper.

Data availability

Data will be made available on request.

Appendix A. Supplementary data

Supplementary data to this article can be found online at https://doi.org/10.1016/j.cej.2022.139006.

References

[1] C.-X. Chen, Z.-W. Wei, T. Pham, P.C. Lan, L. Zhang, K.A. Forrest, S. Chen, A.M. Al-Enizi, A. Nafady, C.-Y. Su, S. Ma, Nanospace engineering of metal-organic frameworks through dynamic spacer installation of multifunctionalities for

efficient separation of ethane from ethane/ethylene mixtures, Angew. Chem. Int. Ed. 60 (17) (2021) 9680–9685.

[2] M. Kang, S. Yoon, S. Ga, D.W. Kang, S. Han, J.H. Choe, H. Kim, D.W. Kim, Y. G. Chung, C.S. Hong, High-throughput discovery of Ni(IN)$_2$ for ethane/ethylene separation, Adv. Sci. 8 (11) (2021) 2004940.

[3] K. Baamran, S. Lawson, A.A. Rownaghi, F. Rezaei, Process evaluation and kinetic analysis of 3D-printed monoliths comprised of CaO and Cr/H-ZSM-5 in combined CO$_2$ Capture-C$_2$H$_6$ oxidative dehydrogenation to C$_2$H$_4$, Chem. Eng. J. 435 (2022) 134706.

[4] S. Lawson, K. Baamran, K. Newport, F. Rezaei, A.A. Rownaghi, Formulation and processing of dual functional adsorbent/catalyst structured monoliths using an additively manufactured contactor for direct capture/conversion of CO$_2$ with cogeneration of ethylene, Chem. Eng. J. 431 (2022) 133224.

[5] L. Li, R.-B. Lin, R. Krishna, H. Li, S. Xiang, H. Wu, J. Li, W. Zhou, B. Chen, Ethane/ ethylene separation in a metal-organic framework with iron-peroxo sites, Science 362 (6413) (2018) 443–446.

[6] P. Zhou, L. Yue, X. Wang, L. Fan, D.-L. Chen, Y. He, Improving ethane/ethylene separation performance of isoreticular metal-organic frameworks via substituent engineering, ACS Appl. Mater. Interfaces. 13 (45) (2021) 54059–54068.

[7] Y. Wang, S. Yuan, Z. Hu, T. Kundu, J. Zhang, S.B. Peh, Y. Cheng, J. Dong, D. Yuan, H.-C. Zhou, D. Zhao, Pore size reduction in zirconium metal–organic frameworks for ethylene/ethane separation, ACS Sustain. Chem. Eng. 7 (7) (2019) 7118–7126.

[8] Y.u. Yin, Z. Zhang, C. Xu, H. Wu, L. Shi, S. Wang, X. Xu, A. Yuan, S. Wang, H. Sun, Confinement of Ag (I) sites within MIL-101 for robust ethylene/ethane separation, ACS Sustain. Chem. Eng. 8 (2) (2020) 823–830.

[9] J.-X. Wang, X.-W. Gu, Y.-X. Lin, B. Li, G. Qian, A novel hydrogen-bonded organic framework with highly permanent porosity for boosting ethane/ethylene separation, ACS Mater. Lett. 3 (5) (2021) 497–503.

[10] Z. Wu, S.-S. Han, S.-H. Cho, J.-N. Kim, K.-T. Chue, R.T. Yang, Modification of resin-type adsorbents for ethane/ethylene separation, Ind. Eng. Chem. Res. 36 (7) (1997) 2749–2756.

[11] H. Thakkar, Q. Al-Naddaf, N. Legion, M. Hovis, A. Krishnamurthy, A.A. Rownaghi, F. Rezaei, Adsorption of ethane and ethylene over 3D-printed ethane-selective monoliths, ACS Sustain. Chem. Eng. 6 (11) (2018) 15228–15237.

[12] P.-Q. Liao, W.-X. Zhang, J.-P. Zhang, X.-M. Chen, Efficient purification of ethene by an ethane-trapping metal-organic framework, Nat. Commun. 6 (2015) 1–9.

[13] K. Adil, Y. Belmabkhout, R.S. Pillai, A. Cadiau, P.M. Bhatt, A.H. Assen, G. Maurin, M. Eddaoudi, Gas/vapour separation using ultra-microporous metal–organic frameworks: insights into the structure/separation relationship, Chem. Soc. Rev. 46 (2017) 3402–3430.

[14] Y. Yang, L. Li, R.-B. Lin, Y. Ye, Z. Yao, L. Yang, F. Xiang, S. Chen, Z. Zhang, S. Xiang, B. Chen, Ethylene/ethane separation in a stable hydrogen-bonded organic framework through a gating mechanism, Nat. Chem. 13 (10) (2021) 933–939.

[15] C.A. Grande, A.E. Rodrigues, Electric swing adsorption for CO$_2$ removal from flue gases, Int. J. Greenh. Gas Control. 2 (2008) 194–202.

[16] T. Chronopoulos, Y. Fernandez-Diez, M.M. Maroto-Valer, R. Ocone, D.A. Reay, CO$_2$ desorption via microwave heating for post-combustion carbon capture, Microporous Mesoporous Mater. 197 (2014) 288–290.

[17] Y. Gomez-Rueda, B. Verougstraete, C. Ranga, E. Perez-Botella, F. Reniers, J.F. M. Denayer, Rapid temperature swing adsorption using microwave regeneration for carbon capture, Chem. Eng. J. 446 (2022) 137345.

[18] H. Li, M.M. Sadiq, K. Suzuki, R. Ricco, C. Doblin, A.J. Hill, S. Lim, P. Falcaro, M. R. Hill, Magnetic metal-organic frameworks for efficient carbon dioxide capture and remote trigger release, Adv. Mater. 28 (9) (2016) 1839–1844.

[19] M. Gholami, B. Verougstraete, R. Vanoudenhoven, G.V. Baron, T. Van Assche, J.F. M. Denayer, Induction heating as an alternative electrified heating method for carbon capture process, Chem. Eng. J. 431 (2022) 133380.

[20] C.A. Grande, R.P.L. Ribeiro, E.L.G. Oliveira, A.E. Rodrigues, Electric swing adsorption as emerging CO$_2$ capture technique, Energy Procedia. 1 (1) (2009) 1219–1225.

[21] P. Mocho, P. Le Cloirec, Regeneration of granular activated carbon by inductive heating-Application in the elimination and recycling of air-born solvents, Stud. Environ. Sci., Elsevier (1994) 251–259.

[22] M.M. Sadiq, K. Konstas, P. Falcaro, A.J. Hill, K. Suzuki, M.R. Hill, Engineered porous nanocomposites that deliver remarkably low carbon capture energy costs, Cell Reports Phys. Sci. 1 (2020) 100070.

[23] M.M. Sadiq, H. Li, A.J. Hill, P. Falcaro, M.R. Hill, K. Suzuki, Magnetic induction swing adsorption: an energy efficient route to porous adsorbent regeneration, Chem. Mater. 28 (2016) 6219–6226.

[24] X. Lin, B. Shao, J. Zhu, F. Pan, J. Hu, M. Wang, H. Liu, In situ electromagnetic induction heating for CO$_2$ temperature swing adsorption on magnetic Fe$_3$O$_4$/N-doped porous carbon, Energy Fuels 34 (11) (2020) 14439–14446.

[25] Q. Al-Naddaf, H. Thakkar, F. Rezaei, Novel zeolite-5A@MOF-74 composite adsorbents with core-shell structure for H$_2$ purification, ACS Appl. Mater. Interfaces 10 (35) (2018) 29656–29666.

[26] Y. Chen, D. Lv, J. Wu, J. Xiao, H. Xi, Q. Xia, Z. Li, A new MOF-505@GO composite with high selectivity for CO$_2$/CH$_4$ and CO$_2$/N$_2$ separation, Chem. Eng. J. 308 (2017) 1065–1072.

[27] J. Wang, G. Zhao, F. Yu, Facile preparation of Fe$_3$O$_4$@MOF core-shell microspheres for lipase immobilization, J. Taiwan Inst. Chem. Eng. 69 (2016) 139–145.

[28] M. Chen, Z. Wang, Y. Liu, J. Chen, J. Liu, D. Gan, Effect of ligands of functional magnetic MOF-199 composite on thiophene removal from model oil, J. Mater. Sci. 56 (4) (2021) 2979–2993.

[29] S. Yadav, R. Dixit, S. Sharma, S. Dutta, K. Solanki, R.K. Sharma, Magnetic metal–organic framework composites: structurally advanced catalytic materials for organic transformations, Mater. Adv. 2 (2021) 2153–2187.

[30] L. Li, Y. Xu, D. Zhong, N. Zhong, CTAB-surface-functionalized magnetic MOF@ MOF composite adsorbent for Cr(VI) efficient removal from aqueous solution, Colloids Surf., A Physicochem. Eng. Asp. 586 (2020) 124255.

[31] C.M. Doherty, D. Buso, A.J. Hill, S. Furukawa, S. Kitagawa, P. Falcaro, Using functional nano-and microparticles for the preparation of metal–organic framework composites with novel properties, Acc. Chem. Res. 47 (2) (2014) 396–405.

[32] A. Van Miltenburg, W. Zhu, F. Kapteijn, J.A. Moulijn, Adsorptive separation of light olefin/paraffin mixtures, Chem. Eng. Res. Des. 84 (5) (2006) 350–354.

[33] M. Hartmann, U. Böhme, M. Hovestadt, C. Paula, Adsorptive separation of olefin/ paraffin mixtures with ZIF-4, Langmuir 31 (45) (2015) 12382–12389.

[34] T. Alghamdi, K.S. Baamran, M.U. Okoronkwo, A.A. Rownaghi, F. Rezaei, Metal-doped K-Ca double salts with improved capture performance and stability for high-temperature CO$_2$ adsorption, Energy Fuels 35 (5) (2021) 4258–4266.

[35] A. Al-Mamoori, S. Lawson, A.A. Rownaghi, F. Rezaei, Improving adsorptive performance of CaO for high-temperature CO$_2$ capture through Fe and Ga doping, Energy Fuels 33 (2) (2019) 1404–1413.

[36] A. Al-Mamoori, H. Thakkar, X. Li, A.A. Rownaghi, F. Rezaei, Development of potassium-and sodium-promoted CaO adsorbents for CO$_2$ capture at high temperatures, Ind. Eng. Chem. Res. 56 (29) (2017) 8292–8300.

[37] H. Guo, X. Kou, Y. Zhao, S. Wang, Q. Sun, X. Ma, Effect of synergistic interaction between Ce and Mn on the CO$_2$ capture of calcium-based sorbent: Textural properties, electron donation, and oxygen vacancy, Chem. Eng. J. 334 (2018) 237–246.

[38] Y. Gong, C. Chen, R.P. Lively, K.S. Walton, Humid ethylene/ethane separation on ethylene-selective materials, Ind. Eng. Chem. Res. 60 (27) (2021) 9940–9947.

[39] S. Pu, J. Wang, L. Li, Z. Zhang, Z. Bao, Q. Yang, Y. Yang, H. Xing, Q. Ren, Performance comparison of metal–organic framework extrudates and commercial zeolite for ethylene/ethane separation, Ind. Eng. Chem. Res. 57 (5) (2018) 1645–1654.

[40] S. Lawson, F. Rezaei, Effects of process parameters on CO$_2$/H$_2$ separation performance of 3D-printed MOF-74 monoliths, ACS Sustain. Chem. Eng. 9 (2021) 10902–10912, https://doi.org/10.1021/acssuschemeng.1c03443.